

The VST ATLAS Quasar Survey III: Halo mass function via quasar clustering and quasar-CMB lensing cross-clustering

Alice M. Eltvedt,¹★ T. Shanks,¹† N. Metcalfe,¹ B. Ansarinejad,² L.F. Barrientos,³

D.N.A. Murphy^{3,4} and D.M. Alexander¹

¹Centre for Extragalactic Astronomy, Department of Physics, Durham University, South Road, Durham, DH1 3LE, UK

²School of Physics, University of Melbourne, Parkville, VIC 3010, Australia

³Instituto de Astrofísica, Facultad de Física, Pontificia Universidad Católica de Chile, Santiago, Chile

⁴Institute of Astronomy, University of Cambridge, Madingley Road, Cambridge CB3 0HA, UK

Accepted XXX. Received YYY; in original form ZZZ

ABSTRACT

We exploit the VST ATLAS quasar/QSO catalogue to perform three measurements of the quasar halo mass profile. First, we make a new estimate of the angular auto-correlation function of $\approx 230,000$ ATLAS quasars with $z_{photo} \lesssim 2.5$ and $17 < g < 22$. By comparing with the Λ CDM mass clustering correlation function, we measure the quasar bias to be $b_Q \approx 2.1$, implying a quasar halo mass of $M_{halo} \approx 8.5 \times 10^{11} h^{-1} M_{\odot}$. Second, we cross-correlate these $z \approx 1.7$ ATLAS quasars with the Planck Cosmic Microwave Background (CMB) lensing maps, detecting a somewhat stronger signal at $4' < \theta < 60'$ than previous authors. Scaling these authors' model fit to our data we estimate a quasar host halo mass of $M_{halo} \approx 8.3 \times 10^{11} h^{-1} M_{\odot}$. Third, we fit Halo Occupation Distribution (HOD) model parameters to our quasar auto-correlation function and from the derived halo mass function we estimate a quasar halo mass of $M_{halo} \approx 2.5 \times 10^{12} h^{-1} M_{\odot}$. We then compare our HOD model prediction to our quasar-CMB lensing result, confirming their consistency. We find that most ($\approx 2/3$) QSOs have halo masses within a factor of ≈ 3 of this average mass. An analysis based on the probability of X-ray detections of AGN in galaxies and the galaxy stellar mass function gives a similarly small mass range. Finally, we compare the quasar halo mass and luminosity functions and suggest that gravitational growth may produce the constant space density with redshift seen in the quasar luminosity function.

Key words: large-scale structure of Universe - quasars: general

1 INTRODUCTION

Quasars are great tracers of large scale structure as they are visible across a wide redshift range and their high bias also makes their clustering easier to detect. In Eltvedt et al. (2024) (hereafter Paper I) we also exploited weak lensing ‘magnification bias’ of quasars to measure the mass profiles of galaxies and clusters of galaxies. But in terms of measuring the masses and halo profiles of quasars themselves, we must turn to the Cosmic Microwave Background (CMB) as the CMB provides a background to all of the observable structures in the universe, including quasars. We can use the deflection of CMB photons to trace the matter density field (e.g. Blanchard & Schneider 1987; Seljak 1996) which, when combined with the QSO clustering measurements, allows the quasar bias to be calculated. We can then evaluate the relationship between this bias and the host dark matter halo mass and place the quasars in a cosmological context. Here we follow the recent works of Geach et al. (2019); Han et al. (2019); Petter et al. (2022, 2023), who argue that the cross-correlation of a CMB lensing convergence map and a quasar sample offers a more direct way of estimating quasar bias than the more commonly used

way of combining standard cosmology assumptions with measurements of the quasar 2-point auto-correlation function (e.g. Croom et al. 2005; Chehade et al. 2016), with a lower level of systematics. So here we aim to measure the halo mass profiles of QSOs from the catalogue of Paper I. These were first used to measure the halo mass profiles of galaxy clusters, galaxies and LRGs via QSO lensing in Paper II and now these QSOs themselves will have their halo mass profiles measured by fitting HODs to the QSO clustering correlation function and then testing this fit using QSO-CMB lensing.

The overall aim therefore is to determine the QSO host halo mass function at $z \approx 1.7$. Previously, the main route to finding QSO halo masses has been by estimating the bias of QSOs through the comparison of the QSO 3-D redshift-space correlation function with an assumed Λ CDM clustering correlation function, and then using the bias-halo mass relation to estimate average halo masses. This then leads to studies investigating, for example, how QSO halo mass may depend on QSO luminosity (Chehade et al. 2016).

Here, we first measure the 2-D angular auto-correlation function of our QSO sample defined in Paper II. This function is independent of redshift space distortions and only one or two authors have previously been able to go this route (e.g. Petter et al. 2023). The high quality of the VST ATLAS QSO samples have allowed us to measure the QSO 2-D angular correlation function and make a new bias and

★ E-mail: aeltvedt@alumni.princeton.edu

† E-mail: tom.shanks@durham.ac.uk

average halo mass estimates in this way. But this route only delivers the average halo mass at a given redshift with no information about e.g. the width of the mass distribution. We therefore proceed to make a more detailed estimate of the QSO halo mass function by fitting QSO HOD models to the QSO auto-correlation function data.

We then go on to use QSO lensing of the CMB to make further tests of the above results. Here, we cross-correlate the ATLAS QSO sample with the *Planck* CMB lensing convergence map. This first allows us to test directly the bias estimated from QSO clustering, free from the assumption of the Λ CDM model, and to make an independent estimate of the QSO average host halo mass via the above bias-halo mass relation. Then, we make a direct measurement of the full QSO host halo mass function by fitting a HOD model to our QSO-*Planck* cross-correlations. Finally, we are able to determine the QSO halo mass function by multiplying the derived QSO HOD with the Λ CDM halo mass function.

The structure of this paper is as follows. In Section 2 we describe the two data catalogues we will be using throughout the paper. In Section 3 we start our analysis by performing an auto-correlation of our QSO sample to measure the clustering amplitude and compare our sample to that of [Petter et al. \(2023\)](#), before deriving both the QSO bias and host halo mass via this ω_{qq} . We then detect the deflection (lensing) of the Cosmic Microwave Background (CMB) ([Planck Collaboration et al. 2018](#)) by our quasar candidates through a cross-correlation of our QSO survey and the *Planck* CMB lensing map (e.g. [Geach et al. 2019](#); [Han et al. 2019](#); [Petter et al. 2022](#)) in Section 4 to also derive a host halo mass via the measurement of the QSO bias from a simple scaling of the halo profile model of [Geach et al. \(2019\)](#). Finally, in Section 5 we fit both our ω_{qq} and ω_{Q-CMB} results with a HOD model to find the best fitting halo mass distribution of our QSO sample. We present our conclusions in Section 6. Throughout, we assume a standard, spatially flat, cosmology with $\Omega_m = 0.3$ and a Hubble constant assumed to be $100 \text{ h km s}^{-1} \text{ Mpc}^{-1}$, with $h=0.7$ unless otherwise stated.

2 DATA

2.1 Quasar Sample

The VST-ATLAS quasar catalogue described in [Paper I](#) has a certain amount of stellar and galaxy contamination to improve completeness. For the purposes of the analyses in this paper, we use a non-photometric redshift restricted version of the QSO sample described in [Paper II](#), which introduces restricted *ugriW1W2* selections to the Priority 1 QSO sample from [Paper I](#), as well as a mask to remove Tycho stars and globular clusters. These selections result in a total of 230914 ATLAS quasar candidates giving us a sky density of 49 deg^{-2} . The photometric redshift distribution of our final QSO sample is shown in Fig. 1, showing a clear peak in the distribution at ≈ 1.8 . Also shown in Fig. 1, is the $dn(z)/dz$ distribution for SDSS quasars to a similar limit in the form of:

$$\left. \frac{dn}{dz} \right|_Q \sim z^{2.56} \exp\left[-\left(\frac{z}{2.02}\right)^{12.76}\right], \quad (1)$$

([Scranton et al. 2005](#)) which, although the model is formally rejected by the data, it still represents a reasonable fit to the shape of our distribution. We therefore use this relation to describe our QSO sample in Section 5.

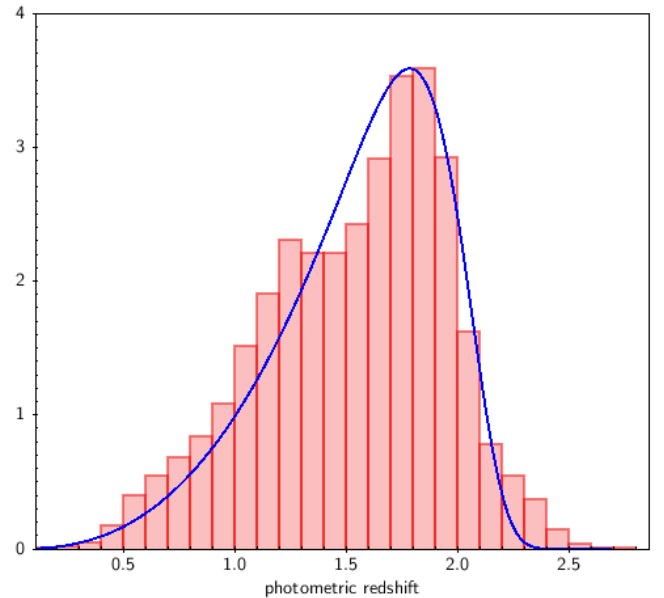


Figure 1. Our VST ATLAS+unWISE QSO sample redshift distribution, $dn(z)/dz$, along with the SDSS $dn(z)/dz$ redshift distribution from [Scranton et al. \(2005\)](#) described by Equation 1, with the y-axis showing the total number of QSOs in the NGC+SGC divided by 7049.4 in order to scale it to the model.

We visually inspect the QSO candidate distribution in the sky to see a relatively flat distribution of candidates across the sky as well as confirming that we have masked out bright stars and globular clusters. This density of candidates is shown in Fig. 2.

2.2 *Planck* CMB Lensing Convergence Map

To perform our cross-correlation, we use the 2018 release of the *Planck* lensing convergence baseline map ([Planck Collaboration et al. 2018](#)), with $n_{\text{side}} = 2048$ and $l_{\text{max}} = 4096$, as described in [Paper II](#). Within the healpy *alm2map* routine, we first smoothed the lensing spherical harmonics, a_{lm} , assuming a Gaussian kernel of FWHM $15'$. After using *alm2map* to convert the CMB-only minimum variance a_{lm} estimates of the lensing signal to an RA +Dec file with coordinates of the Healpix pixel centers, we apply the lensing mask provided by the [Planck Collaboration et al. \(2018\)](#) to the CMB data and select two areas that overlap our $\sim 4700 \text{ deg}^2$ QSO sample, shown in Fig. 2. The resulting lensing convergence maps we use in our work are shown in Fig. 3. Note that here we are following the method of [Geach et al. \(2019\)](#) except that we do not project the convergence map onto a tangential (Zenithal Equal Area) flat sky projection, since our aim is to apply the cross-correlation technique directly without, as an intermediate step, producing images of the convergence maps around each quasar for stacking.

3 QSO ANGULAR CORRELATION FUNCTION

The QSO angular correlation function, $w_{qq}(\theta)$, measures the strength of quasar clustering as a function of the angular separation, θ , of quasars on the sky. The large width of the QSO $n(z)$, typically spanning the range $1 \lesssim z \lesssim 2$, tends strongly to dilute the QSO clustering in 3-D, making w_{qq} hard to detect against the random

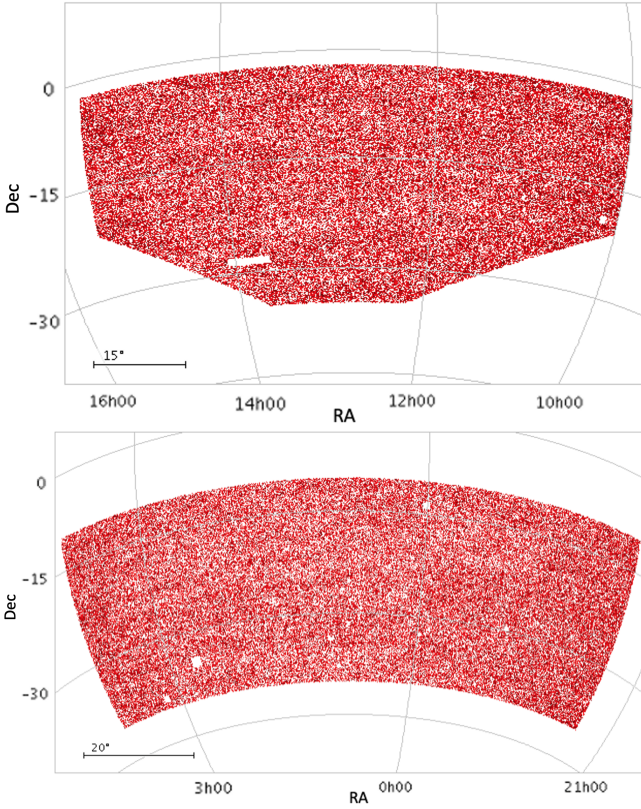


Figure 2. Sky density maps of the VST ATLAS QSO candidates in the NGC (above) and the SGC (below) used in this paper. Areas of higher density are shaded in a darker red whereas lower density areas are lighter.

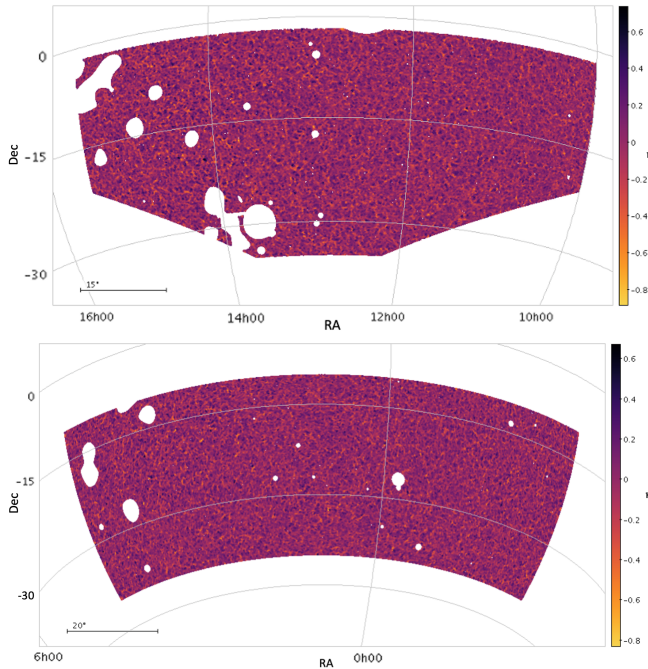


Figure 3. The CMB lensing convergence map in the NGC (above) and SGC (below).

noise and low-level systematics. Therefore QSO clustering has traditionally only been measured using QSO redshift surveys like 2dF (Croom et al. 2005) which do not suffer from projection effects. Only recently have QSO angular correlation functions been measured (e.g. Petter et al. 2023) since they demand large sky areas to remove statistical noise and careful treatment of QSO survey systematics. So a significant detection of w_{qq} also represents a challenging test of the reliability of a quasar survey.

Once detected, w_{qq} offers an alternative route to the quasar spatial correlation function, $\xi(r)$, uncontaminated by redshift space distortion effects (Kaiser 1987). The first aim then is usually to compare the clustering amplitudes of the QSO and underlying matter to determine the QSO linear bias, defined by $b_Q = \sqrt{\xi_{qq}/\xi_{mm}}$ where ξ_{mm} is the spatial correlation function of the matter distribution. The halo mass of the QSO host galaxy can then be estimated via the QSO bias - halo mass relation. Although the quasar angular correlation function, w_{qq} , the projected version of ξ_{qq} , is only detectable at lower S/N than ξ_{qq} , it has the advantage of being unaffected by z-space distortions and so provides a viable alternative route to determining quasar halo masses.

3.1 Method

We perform the autocorrelation of our QSO sample using the Correlation Utilities and Two-point Estimates (CUTE) code Alonso (2012). As described in Paper II, CUTE calculates the autocorrelation by using the normalized Landy & Szalay (1993) estimator, defined as:

$$\omega_{QQ}(\theta) = \frac{D_Q D_Q - D_Q R_Q - R_Q R_Q}{R_Q R_Q}, \quad (2)$$

Here the number of randoms R_Q are always $> 10\times$ larger than the number of quasars, D_Q , i.e. > 2309140 for the full quasar sample. We check the output generated by the Landy-Szalay estimator by manually checking the individual outputs needed to calculate the angular cross-correlation. The standard errors of the cross-correlation are estimated by using the field-field error defined as:

$$\sigma_{\bar{\omega}}(\theta) = \frac{\sigma_{N_s-1}}{\sqrt{N_s}} = \sqrt{\frac{\sum(\omega_i(\theta) - \bar{\omega}_i(\theta))^2}{N_s^2 - N_s}}, \quad (3)$$

where $N_s = 8$, made up of 4 regions of approximately equal area taken from each of the NGC and SGC quasar sub-samples (see Fig. 1 of Paper II).

Our QSO autocorrelation result is shown in Fig. 4 alongside the angular autocorrelation measurements obtained by Petter et al. (2023), who split their sample up into unobscured and obscured QSOs. Here we see that both of the Petter et al. (2023) samples display a steeper angular autocorrelation, especially at small $\theta < 0.5$ scales, where the 1-halo term dominates. The sample used by Petter et al. (2023) is a WISE selected QSO sample, which is then matched to the DESI DR9 r -band (Dey et al. 2019). This has a magnitude limit of $r \sim 24$. The $r - W2$ cut made in their sample to define the obscured and unobscured samples is shown in their Figure 1, and the redshift distributions of the resulting samples are shown in their Figure 3 (with distributions ranging from $0 \lesssim z \lesssim 3.5$). The $n(z)$ distribution of obscured QSOs can be seen to be broader with a less distinct peak than our QSO $n(z)$ distribution in Fig. 1.

3.2 Limber's projection formula

We fit all three autocorrelations via Limber's approximate projection formula (Limber 1953) to translate the 2-D angular correlation function, $\omega(\theta)$ to the 3-D spatial correlation function, $\xi(r)$. If $\xi(r)$ is a power-law, $\xi(r) = (r/r_0)^{-\gamma}$, then $w(\theta)$ is also a power law of the form, $w(\theta) = (\theta/\theta_0)^{1-\gamma}$. Then, knowing the amplitude (θ_0) and slope ($1 - \gamma$) of the 2-D correlation function, the 3-D clustering amplitude (r_0) can be obtained via Limber's formula for each of the QSO samples, using the binned $n(z)$ shown in Fig. 1. Previous studies, such as Phillipps et al. (1978) and Peebles (1980), have shown this approximation to be accurate at small angular scales below a few degrees separation if the power law is an accurate descriptor of $\xi(r)$. We see in Fig. 4 that our QSO correlation function gives a clustering amplitude of $r_0 = 5.2 \text{ h}^{-1} \text{ Mpc}$, with $\gamma = -1.8$, similar to the clustering amplitude of galaxies. The unobscured and obscured QSOs from Petter et al. (2023) give $r_0 = 6.0$ and $7.9 \text{ h}^{-1} \text{ Mpc}$ respectively. We are able to use this clustering amplitude in the following section in order to estimate the QSO bias, and therefore derive the halo mass.

Although our QSO sample seems to have a higher angular clustering amplitude in Fig. 4, this best-fit 3-D clustering amplitudes, r_0 , would indicate the opposite. This occurs because the ATLAS QSO $n(z)$ has a smaller width than the $n(z)$'s of the Petter et al. (2023) QSO samples, shown in their Figure 3. If a QSO sample genuinely has a higher 3-D clustering amplitude, this would imply a higher QSO halo bias. But it could also indicate that the QSO samples of Petter et al. (2023) have lower star contamination or they have assumed a QSO $n(z)$ that is too wide for their actual $n(z)$. In addition, the samples of Petter et al. (2023) show a steeper correlation function at small scales which may indicate a contribution from a 1-halo term than if the correlation function followed a pure power-law. So to understand the form of the ATLAS QSO correlation function in more detail, including the relative contributions of the 1- and 2-halo terms, in Section 5 we shall fit more sophisticated HOD models to our results.

3.3 QSO bias and halo mass via w_{qq}

We now compare our measurement of w_{qq} (deprojected via Limber's formula) to the Λ CDM matter clustering correlation function at $z \approx 1.7$ to estimate the QSO bias at this redshift. Following Croom et al. (2005), we make this comparison by integrating over $\xi(r)$ out to $r=20\text{h}^{-1}\text{Mpc}$ to form ξ_{20} . This $0 < r < 20\text{h}^{-1}\text{Mpc}$ range is chosen so that it is dominated by the linear regime at $r > 5\text{h}^{-1}\text{Mpc}$ and where $\xi(r)$ can be approximated by a power-law:

$$\xi_{20} = 3/20^3 \int_0^{20} \xi(r)r^2 dr = 3/20^3 \int_0^{20} (r/r_0)^{-\gamma} r^2 dr \quad (4)$$

Here we have already assumed a power law form for $\xi(r)$ with power-law slope, $-\gamma$, and scale length, r_0 . We note that $r_{\text{comoving}} = 20\text{h}^{-1}\text{Mpc}$ at $z = 1.7$ corresponds to $\theta = 20'.8$ (see Figs. 4 and 8).

Now, approximating w_{qq} by a power-law of slope $1 - \gamma = -0.67$ and applying Limber's formula, we find $r_0 = 5.3 \pm 0.1\text{h}^{-1}\text{Mpc}$ which from eq (4) gives $\xi_{20} = 0.25 \pm 0.01$ for our QSOs. A Λ CDM matter power spectrum implies $\xi_{20} = 0.235$ for the matter at $z = 0$. Assuming a linear gravitational growth factor of $D(z = 1.7) = 2.033$ between $z = 1.7$ and $z = 0$ then gives $\xi_{20} = 0.235/2.033^2 = 0.057$ for the matter at $z = 1.7$. The QSO bias

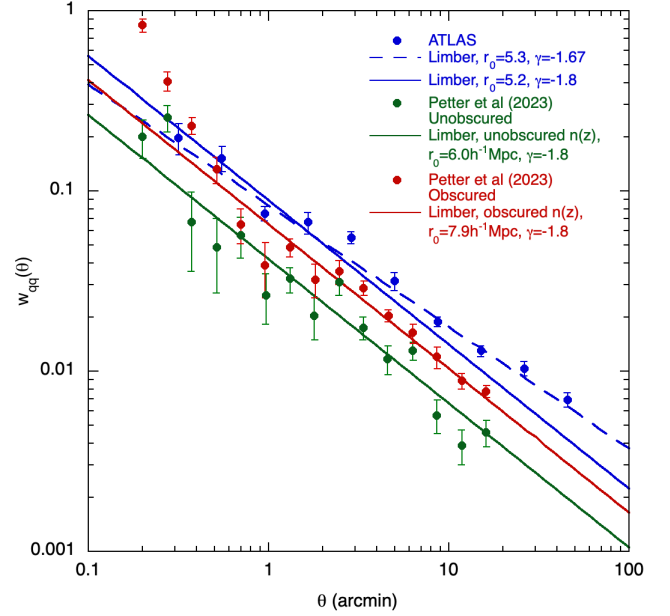


Figure 4. We show the autocorrelation function of our ATLAS QSO sample along with the unobscured and obscured QSO samples of Petter et al. (2023). Limber's formula over full redshift range of our ATLAS QSO sample gives $r_0 = 5.2 \text{ h}^{-1} \text{ Mpc}$. The Limber formula predictions of $r_0 = 6.0, 7.9 \text{ h}^{-1} \text{ Mpc}$ for the unobscured and obscured Petter et al. (2023) samples are also shown, based on their self-consistent redshift distributions. All w_{qq} models assume power-laws for the 3-D $\xi(r)$ with slope $\gamma = -1.8$, along with one better fit model with $r_0 = 5.3 \text{ h}^{-1} \text{ Mpc}$ and slope $\gamma = -1.67$ for our QSO w_{qq} .

at $z = 1.7$ is $b_Q = \sqrt{(0.25/0.057)} = 2.09 \pm 0.09$. Then, following eqs. (13-17) of Chehadé et al. (2016) we derive the bias-mass relation for QSOs at our average QSO redshift, $z = 1.7$, as shown in Fig. 5. From that, we estimate a mean QSO halo mass of $M_{\text{halo}} = 8.5 \pm 3 \times 10^{11} \text{ h}^{-1} M_{\odot}$ at this redshift.

4 QSO-CMB LENSING CROSS-CORRELATION

The cross correlation of our QSO catalogue with the Planck CMB lensing convergence map (Planck Collaboration et al. 2018) is an independent method towards determining the QSO bias and the QSO halo mass.

4.1 Quasar-CMB Lensing Cross-Correlation Model

We first perform our analysis using the model described in the studies of Geach & Peacock (2017), Geach et al. (2019), and Petter et al. (2022). The model includes a lensing convergence contribution made by a 1-halo and a 2-halo term. Similarly to the equation used in the Williams & Irwin (1998) model from Paper II, the convergence due to the 1-halo term is defined as:

$$\kappa_1(R) = \frac{\Sigma(R)}{\Sigma_{\text{crit}}} \quad (5)$$

where $\Sigma(R)$ is the projected mass surface density given an NFW density profile, and Σ_{crit} is the critical surface density. Here, the projected mass surface density is:

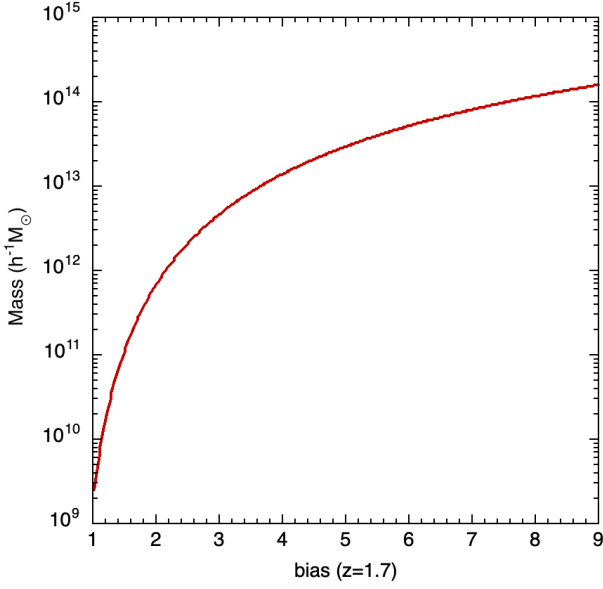


Figure 5. The calculated bias-mass relation for QSOs at redshift $z=1.7$ based on equations 13-17 of [Chehade et al. \(2016\)](#).

$$\Sigma(R) = 2 \int_R^\infty \frac{r\rho(r)}{\sqrt{(r^2 - R^2)}} dr \quad (6)$$

The 2-halo term is described by:

$$\kappa_2(\theta) = \frac{\bar{\rho}(z)}{(1+z)^3 \Sigma_{crit} D^2(z)} \int \frac{ldl}{2\pi} J_0(l\theta) b_h \Delta(k, z) \quad (7)$$

where J_0 is a Bessel function of the zeroth order, $D(z)$ is the angular diameter distance, $\Delta(k, z)$ is the linear matter power spectrum, $\bar{\rho}(z)$ is the average density of the Universe at z and b_h is the quasar bias for a halo of mass M_h . Then, the final model for the lensing convergence is:

$$\langle \kappa \rangle = \int dz (\kappa_1 + \kappa_2) dn/dz \quad (8)$$

The lensing convergence results obtained by [Geach et al. \(2019\)](#) are shown in their Figure 3. There we see the radial profile of the quasar stacked convergence along with the best fitting lensing model as a solid line. The model includes the 1- and 2-halo contribution to the lensing signal, although at scales of $\theta > 5'$, the 1-halo term is mostly filtered out. A similar approach is taken by [Petter et al. \(2022\)](#), where their Figure 5 shows a comparable model. Both [Geach et al. \(2019\)](#) and [Petter et al. \(2022\)](#) filter and stack their model (based on Equation 8) in order to mimic the filtering done on the CMB and QSO data. Therefore, the final model does fall below zero at $\sim \theta = 40'$ (see Fig. 6), even though neither the 1- or 2-halo term components do so. Below, we shall be simply scaling the 2-halo term of the model presented in both [Geach et al. \(2019\)](#)

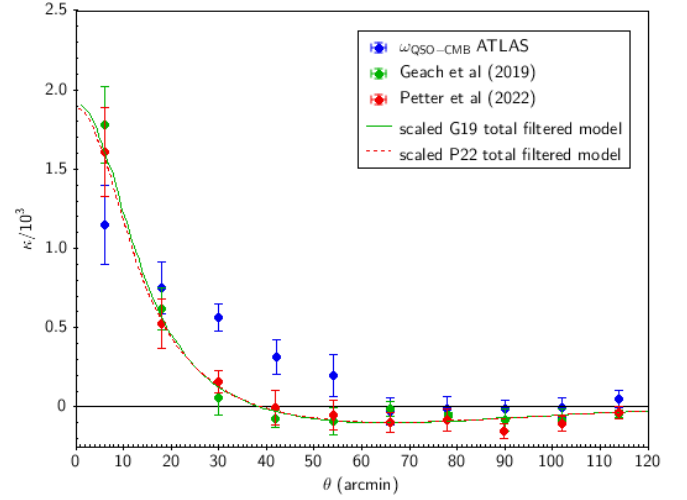


Figure 6. We show our QSO-CMB Lensing cross-correlation result in blue along with the result obtained by [Geach et al. \(2019\)](#) and [Petter et al. \(2022\)](#), in green and red respectively. The total filtered model, scaled by a factor of 0.8, from [Geach et al. \(2019\)](#) is shown as a green line. The total filtered model, scaled by a factor of 0.85, from [Petter et al. \(2022\)](#) is shown as a dashed red line.

and [Petter et al. \(2022\)](#) for a first order calculation of our QSO bias.

The CMB lensing convergence denoted by κ is a projection of a 3D density field. The quasar density is also a projection of a 3D density field. We convert these 3D projections into angular comoving distances in order to perform angular correlations. In our analysis we assume that we have the same absolute magnitude range as [Chehade et al. \(2016\)](#). We also use a comparable quasar sample to [Geach et al. \(2019\)](#) and [Petter et al. \(2022\)](#). However, our photometric redshifts are less accurate and therefore it may not be worth splitting into redshift and/or magnitude bins to perform further analysis.

4.2 Quasar-CMB Lensing Cross-Correlation Results

Results of the cross-correlation we perform between our quasar sample and the Planck CMB Lensing map can be seen in Fig. 6. We show our results along with the results found by [Geach et al. \(2019\)](#) and [Petter et al. \(2022\)](#). We note that the errors on our results are reasonably comparable to both these authors. The main difference between the two results is between $30 - 60'$ where our results are higher. So, while the models of [Geach et al. \(2019\)](#) and [Petter et al. \(2022\)](#) fit their data at $\theta < 60'$ with values of reduced $\chi^2 \approx 4 \times 10^{-4}$, (with only appeal left to a statistical fluctuation to explain this small χ^2 value, given the consistency between their errors and ours), these (scaled) models are rejected as fits to our result, both giving reduced $\chi^2 \approx 8.4$ over the same $\theta < 60'$ range. Comparing the observed results of ourselves and [Geach et al. \(2019\)](#) directly and so taking their errors into account, we still find a reduced $\chi^2 = 3.2$ over the full $\theta < 90'$ range. The reason for this discrepancy is unclear.

We first determine the QSO bias found with our results by scaling the total filtered model determined by [Geach et al. \(2019\)](#), indicated on Figure 3 of their paper, as well as the filtered total model from [Petter et al. \(2022\)](#), indicated on Figure 5 of their paper, to our data. Both models include the 1- and 2-halo term described in the previous section and are filtered in the same way as their data. We look at the $0' < \theta < 60'$ range as our data falls below $\kappa = 0$ at

larger scales. The reason for the negative cross-correlations seen at $40 < \theta < 60'$ by the other authors but not by ourselves is unclear. The main procedural difference was that we did not make a tangential plane projection to the lensing data before stacking, so that may be the cause. Additionally, there are most likely more systematics at larger scales, despite the errors being smaller. We also note that this χ^2 fit and associated errors are only approximate as they do not take into account covariance between data points.

Upon scaling the models, we find that the total model from Geach et al. (2019) has a best χ^2 fit for a scale of 0.8. Therefore, scaling the measured quasar halo bias of $b_h = 2.7 \pm 0.3$ at $z = 1.7$ found by Geach et al. (2019) by 0.8, gives us a QSO halo bias of $b_h = 2.16 \pm 0.43$ at $z = 1.7$. For the total model of Petter et al. (2022), we find a best fit scaling factor of 0.85. Through scaling their QSO halo bias of $b_h = 2.35 \pm 0.02$ by 0.85 we can infer a QSO bias value of $b_h = 2.0 \pm 0.17$ for our data. The bias to mass relation described in Section 3.3 then indicates a host halo mass of $9.17 \times 10^{11} h^{-1} M_\odot$ for $b_h = 2.16$ and $6.71 \times 10^{11} h^{-1} M_\odot$ for $b_h = 2.0$. We therefore average these two bias measurements determined via scaling the total models of Geach et al. (2019) and Petter et al. (2022) to get $b_h = 2.08 \pm 0.3$, with a host halo mass of $8.3 \pm 3 \times 10^{11} h^{-1} M_\odot$.

In Figure 14 of Chehade et al. (2016), they show the bias they determined as a function of redshift and absolute magnitude. In Fig. 7, we add to Fig. 14 of Chehade et al. (2016) our bias measurement of $b_h = 2.08 \pm 0.3$, shown as a red point, and the $b_h = 2.35 \pm 0.02$ value found by Petter et al. (2022) in green. The bias result of $b_h = 2.7 \pm 0.3$ at $z = 1.7$ found by Geach et al. (2019) is shown as a blue point. We also show the bias value of $b_h = 2.09$ determined via the QSO auto-correlation in Section 3.3 in yellow. The dotted black line represents the bias result determined by Chehade et al. (2016) and the bias result from 2QZ (Croom et al. 2005) is shown as a dashed black line. Also in the figure is the measurement of the quasar halo bias from the BOSS survey (Dawson et al. 2013) determined by Eftekharzadeh et al. (2015). The solid grey line represents the evolution for a halo of mass $2 \times 10^{12} h^{-1} M_\odot$. From this figure, we see that the quasar halo bias measured by Geach et al. (2019) is in line with the bias measured 2QZ, but falls above the bias found by Chehade et al. (2016) (the black dotted line). The bias found by Petter et al. (2022) is in line with the result found by Chehade et al. (2016). We see that our bias measurements fall slightly below all of these results but are still within reasonable agreement. We note that in applying this scaling process, we have effectively assumed the same redshift distribution, dn/dz , for ourselves, Petter et al. (2022), and Geach et al. (2019). Uncertainties in photometric redshifts and the ranges used for the analyses may thus also account for some of the discrepancies between these results.

Overall there seems to be good agreement between the quasar-CMB lensing results of Geach et al. (2019), Petter et al. (2022), and the results from Chehade et al. (2016) which are derived from QSO clustering. The bias, and associated host halo mass results we find via QSO-CMB lensing are also in good agreement when scaling to the total model. We use this as a first order estimate of our data and continue forward by fitting a separate HOD model to our results. These QSO bias and host halo mass measurements, along with the measurements found in Section 5, are summarized in Table 1.

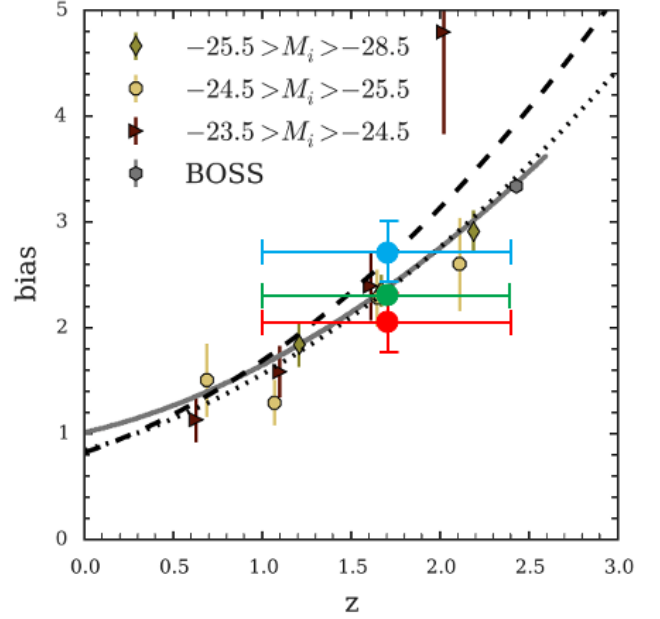


Figure 7. The quasar halo bias as a function of redshift, taken from Figure 14 of Chehade et al. (2016). We show the b_h value of 2.7 ± 0.3 at $z = 1.7$ found by Geach et al. (2019) in blue and the $b_h = 2.35 \pm 0.02$ value found by Petter et al. (2022) in green. Our bias value of $b_h = 2.08 \pm 0.3$ estimated via scaling of the 2-halo model is shown together with our bias value of $b_h = 2.09$ determined via ω_{qq} in Section 3.3 in red. The dotted black line represents the bias result determined by Chehade et al. (2016) and the bias result from 2QZ (Croom et al. 2005) is shown as a dashed black line. The solid grey line represents the evolution for a halo of mass $2 \times 10^{12} h^{-1} M_\odot$.

Table 1. Summary of results for QSO bias b_Q and halo mass M_{halo} . Rows 1-3 contain our VST ATLAS results via (1) the bias from the QSO angular autocorrelation function, (2) the bias fitted to the QSO-CMB lensing cross-correlation function and (3) a HOD model fitted jointly to the above two. Also shown are previous results from Croom et al. (2005), Chehade et al. (2016), Geach et al. (2019), Petter et al. (2022) and Petter et al. (2023).

$z = 1.7$ QSO Sample + Method	bias (b_h)	Mass ($10^{12} h^{-1} M_\odot$)	log Mass ($h^{-1} M_\odot$)
ATLAS ACF w_{qq}	2.09 ± 0.09	0.85 ± 0.3	11.9 ± 0.04
ATLAS CMB Lensing $w_{q\kappa}$	2.08 ± 0.3	$0.83^{+0.8}_{-0.5}$	11.9 ± 0.4
ATLAS HOD $w_{qq} + w_{q\kappa}$	$2.60^{+0.30}_{-0.23}$	$2.5^{+1.5}_{-0.9}$	12.4 ± 0.2
Croom05 z-space ACF	2.17 ± 0.09	1.2 ± 0.2	12.1 ± 0.08
Chehade16 z-space ACF	2.34 ± 0.35	2.0 ± 1.0	12.3 ± 0.4
Geach19 CMB Lensing	2.7 ± 0.3	$4.0^{+2.3}_{-1.5}$	12.6 ± 0.2
Petter22 CMB Lensing	2.35 ± 0.02	3.0 ± 0.4	12.5 ± 0.05
Petter23 HOD $w_{qq} + w_{q\kappa}$	2.3 ± 0.5	4.0 ± 1.4	12.6 ± 0.2

5 HOD MODEL VIA QSO AUTO-CORRELATION AND QSO-CMB LENSING CROSS-CORRELATION

5.1 HOD model

We utilize the CHOMP package based on the work of Jain et al. (2003) and Scranton et al. (2005) and available on the CHOMP GitHub (CHOMP; Morrison, Scranton, and Schneider), to fit HOD models to both the auto-correlation, w_{qq} , of our QSO sample as well as the QSO-CMB lensing convergence map cross-correlation, $w_{g\kappa}$. To check the CHOMP methodology, we first supplied CHOMP with

the HOD model parameters of [Petter et al. \(2023\)](#). However, in the case of the QSO correlation function, we found that CHOMP could not reproduce the w_{qq} results of [Petter et al. \(2023\)](#), assuming their HOD parameters. In this case, we used the alternative HaloMod package ([Murray et al. 2021](#)) to predict the [Petter et al. \(2023\)](#) 3-D $\xi(r)$ and then input this into Limber’s formula using Eq.(13) of [Phillipps et al. \(1978\)](#). The resulting w_{qq} was found to agree with [Petter et al. \(2023\)](#) and the same procedure was then used to fit our ATLAS w_{qq} .

For the 1-halo term of QSO and matter clustering, we assume a [Navarro et al. \(1996\)](#) NFW model, to predict the projected, lensed mass profile, w_{qm} and then w_{qk} . CHOMP also assumes that halo concentration is a function of halo mass with the functional form $c(m) \approx 9(m/m^*)^{-0.13}$ taken from [Bullock et al. \(2001\)](#). For the 2-halo term, CHOMP assumes the form given in eq. (6) of [Jain et al. \(2003\)](#) with a bias model from [Tinker et al. \(2010\)](#), etc. CHOMP and HaloMod both allow use of the 5-parameter HOD model of [Zheng & Weinberg \(2007\)](#) to fit the 2-point auto-correlation function. For all HOD models, we assume a Λ CDM cosmological model with the matter density $\Omega_M = 0.3 - 0.046$, baryon density $\Omega_b = 0.046$ and $\Omega_\Lambda = 0.7$. We assume adiabatic Gaussian primordial density fluctuations with a power-law index of the spectrum $n_s = 0.96$. The r.m.s. matter density fluctuation is assumed to be $\sigma_8 = 0.8$. The Hubble constant we use throughout is $h = 0.7$. Finally, we define the QSO halo redshift to be at $z = 1.7$ and the CMB at redshift $z = 1100$. Then we fit the HOD parameters: the minimum halo mass scale, $\log M_{min}$, the minimum mass scale softening width, $\sigma_{\log M}$, for the central galaxies, the satellite cut-off mass scale, $\log M_0$, the satellite HOD power-law normalization, $\log M_1$ and its slope, α , at high halo masses.

5.2 QSO autocorrelation

In Fig. 8, we compare our observed QSO correlation function, w_{qq} , to our fitted HOD (solid blue line), with parameters, $\log M_{min} = \log M_0 = 12.2$, $\log M_1 = 13.28$, $\sigma_{\log M} = 0.4$ and $\alpha = 0.7$. Also shown as the solid red line is the HOD fit from [Petter et al. \(2023\)](#) for their unobscured QSO sample, with parameters $\log M_{min} = \log M_0 = 12.4$, $\log M_1 = 13.5$, $\sigma_{\log M} = 0.4$ and $\alpha = 0.7$. This model is rejected by our data to $\theta < 15'$ with a reduced χ^2 of 7.2. We see that our HOD model has slightly reduced mass parameters due to the ATLAS w_{qq} having a lower amplitude ($r_0 = 5.2 \text{ h}^{-1} \text{ Mpc}$) than the unobscured QSO w_{qq} of [Petter et al. \(2023\)](#) that has $r_0 = 6.0 \text{ h}^{-1} \text{ Mpc}$, assuming a $\gamma = -1.8$ power-law form for $\xi(r)$ in both cases (as noted in Sec. 3.2). Our HOD fits the data to $\theta < 15'$ with a reduced χ^2 of 1.79.

5.3 QSO-CMB cross-correlation

We next test these two HOD models for internal and external consistency using the QSO-CMB lensing convergence map cross-correlation function. As we see some discrepancy with regards to various parameter fits for the QSO autocorrelation, we use the QSO-CMB cross-correlation as an independent method to measure the host halo masses. Here, we expand upon the results described in Section 4.2 to compare the predictions of the above two HOD models to our QSO-CMB cross correlation results. We note that at the $6'$ resolution of the Planck lensing map, our cross-correlation analysis will mainly be sensitive to the 2-halo term of QSO clustering.

We see in Fig. 9 that our observed CMB lensing cross-correlation function is in good agreement with our HOD model, with the model

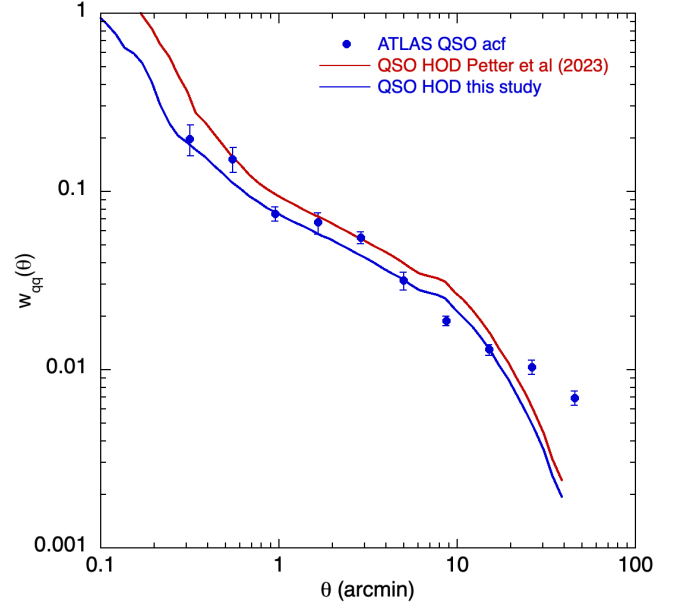


Figure 8. The ATLAS $17 < g < 22$ QSO angular auto-correlation function, w_{qq} , compared to our $1 < z < 2.2$ HOD model (solid blue line) with parameters: $\log(M_{min}) = 12.2$, $\sigma_{\log M} = 0.4$, $\log(M_0) = 12.2$, $\log(M_1) = 13.28$ and $\alpha = 0.7$. The red line shows the unobscured QSO HOD model of [Petter et al. \(2023\)](#) with parameters: $\log(M_{min}) = 12.42$, $\sigma_M = 0.4$, $\log(M_0) = 12.42$, $\log(M_1) = 13.28$ and $\alpha = 0.7$. Both HOD models assume standard Λ CDM parameters with $h = 0.7$ and $\sigma_8 = 0.8$.

giving a value of reduced $\chi^2 = 1.04$ when fitted over the full θ range shown. As previously noted in Section 4.2 our observational results are only in approximate agreement with the results of [Geach et al. \(2019\)](#) and [Petter et al. \(2022\)](#), since our cross-correlation data points are significantly higher than the other two at $10 < \theta < 60'$. This increased amplitude of our results then appears to be reflected in the HODs derived from the ATLAS and [Petter et al. \(2023\)](#) w_{qq} results, as discussed in Section 5.4 below.

5.4 Halo mass of QSOs

In Fig. 10(a) we show our QSO HOD in blue, using the same parameters as in Fig. 8, alongside the [Petter et al. \(2023\)](#) HOD in red, as a function of halo mass, i.e. the halo mass function. In Fig. 10(b) we show the QSO space density as a function of halo mass formed by multiplying the halo mass function by our HOD model and that of [Petter et al. \(2023\)](#). Averaging over these two distributions we find that the average QSO halo mass is $\log M_{eff} = 12.39 (h^{-1} M_\odot)$ for our HOD and $\log M_{eff} = 12.90 (h^{-1} M_\odot)$ for the HOD of [Petter et al. \(2023\)](#). We note that this latter value calculated by ourselves is somewhat higher than the $\log M_{eff} = 12.6 (h^{-1} M_\odot)$ found by [Petter et al. \(2023\)](#) based on their $b_{eff} = 2.25$. Otherwise we note that our lower ($\approx 3\times$) average QSO halo masses are in line with our w_{qq} having a lower scale length of $r_0 = 5.2 \text{ h}^{-1} \text{ Mpc}$ compared to the $r_0 = 6.0 \text{ h}^{-1} \text{ Mpc}$ measured by [Petter et al. \(2023\)](#) for their unobscured QSO sample. Also the results we obtain from the HOD analyses are generally slightly larger than when estimating halo masses directly from w_{qq} and b_Q . However, in terms of the QSO-CMB lensing results in Fig. 9, we do find a larger observed amplitude at $\theta > 10'$ than [Geach et al. \(2019\)](#) for this cross-correlation which is well fitted by our HOD model. The lower cross-correlation

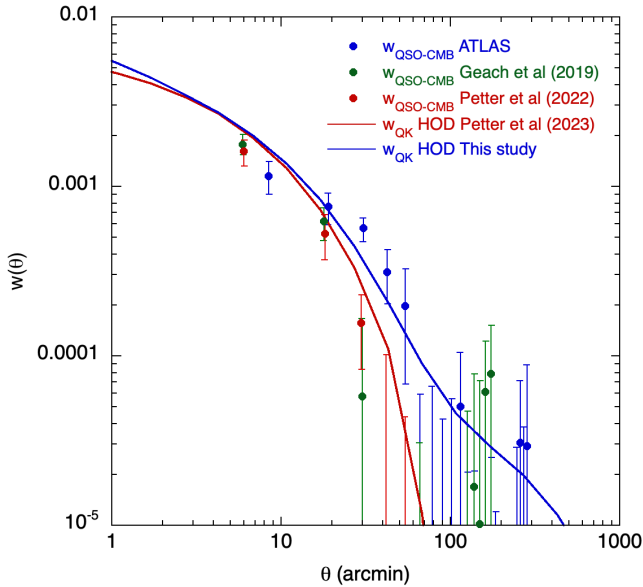


Figure 9. The ATLAS QSO-Planck CMB Lensing Map angular cross-correlation function, $w_{QSO-CMB}$, compared to the results of Geach et al. (2019) and Petter et al. (2022). The solid blue line represents our $1 < z < 2.2$ QSO HOD model previously shown in Fig. 8 with the same HOD parameters as detailed there. The solid red model represents the HOD model of Petter et al. (2023) again as shown in Fig. 8. Both models again assume standard Λ CDM parameters with $h = 0.7$ and $\sigma_8 = 0.8$.

at $\theta > 10'$ observed by Petter et al. (2023) is also well fitted by their HOD model. So the HOD models seem internally consistent between w_{qq} and $w_{QSO-CMB}$. The HODs also seem externally consistent, given the similarities in halo mass function and average halo masses between Petter et al. (2023) and ourselves.

Working directly from our QSO halo mass function in Fig. 10 (b), we find that the average halo mass at $z = 1.7$ is $\log M_{eff} = 12.4$. We further note that our $\log M_{eff} = 12.4$ QSO HOD estimate for the average QSO halo mass is higher than the $\log M = 11.9$ QSO halo mass found from the $b_Q = 2.09$ bias implied by the ratio of the QSO and matter auto-correlation functions (see Section 3.3). It is also larger than the halo mass estimated at $M = 2.58 \pm_{0.36}^{0.39} \times 10^{12} h^{-1} M_\odot$ i.e. $\log M = 11.9$ from the bias of $b_Q = 2.08 \pm 0.3$ we found by scaling the QSO CMB lensing result of Geach et al. (2019) in Section 4.2, shown in Table 1.

From our HOD model in Fig. 10 (b) we see that the QSO mass function shows a steep fall away from $\log M_{min} = 12.2$. Indeed, we calculate that 67% of these $z = 1.7$ QSOs lie in the small halo mass range $12.2 < \log M < 13.2$. Thus it is not unreasonable to say that most QSOs have roughly the same halo mass. This result has been noted before by Shanks et al. (2011) who compared the increasingly faint SDSS, 2QZ and 2SLAQ measurements of the redshift-space correlation $\xi(s)$ and found no dependence of the QSO clustering amplitude on QSO luminosity. Chehade et al. (2016) in the 2QDES pilot survey reached even fainter magnitudes and confirmed this luminosity independence over an order of magnitude (i.e. $\approx 10\times$) in luminosity and over the full $0 < z < 2.5$ redshift range. Since QSO clustering is luminosity independent the implication may be that QSO halo mass and then QSO black hole mass are also luminosity and redshift independent. Here our HOD model now shows that despite the large luminosity range shown by QSOs at fixed redshift (e.g.

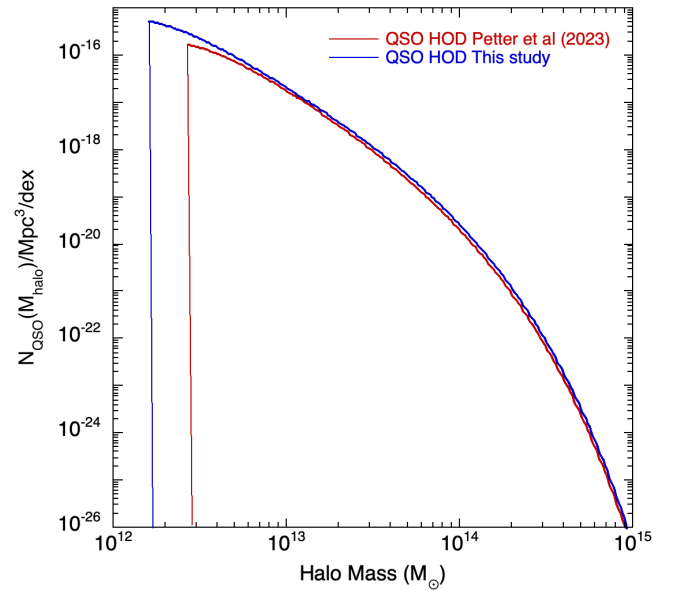
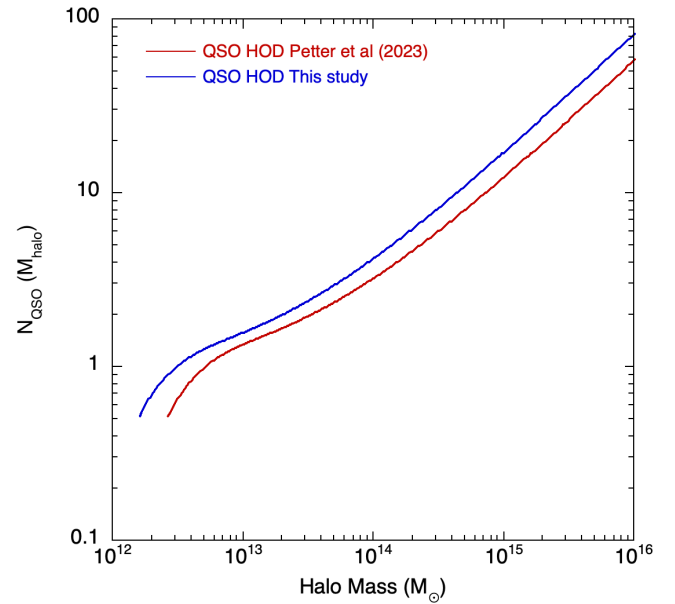


Figure 10. (a) The QSO HOD as a function of halo mass. The solid blue line represents our $1 < z < 2.2$ QSO HOD model previously shown in Fig. 8 with the same HOD parameters as detailed there. The solid red model represents the HOD model of Petter et al. (2023) again as shown in Fig. 8. (b) The QSO space density as a function of halo mass formed by multiplying the halo mass function by a HOD model. The solid blue line represents our $1 < z < 2.2$ QSO HOD model previously shown in Fig. 8 with the same HOD parameters as detailed there. The solid red model represents the HOD model of Petter et al. (2023) again as shown in Fig. 8.

$z \approx 1.7$), the range of halo and hence black hole masses covered is actually very small. This supports the idea that most QSOs have the same black hole mass.

5.5 QSO halo mass and stellar mass functions compared

Further supporting evidence for this hypothesis comes from the X-ray survey in the PRIMUS field, analysed by Aird et al. (2012). Their

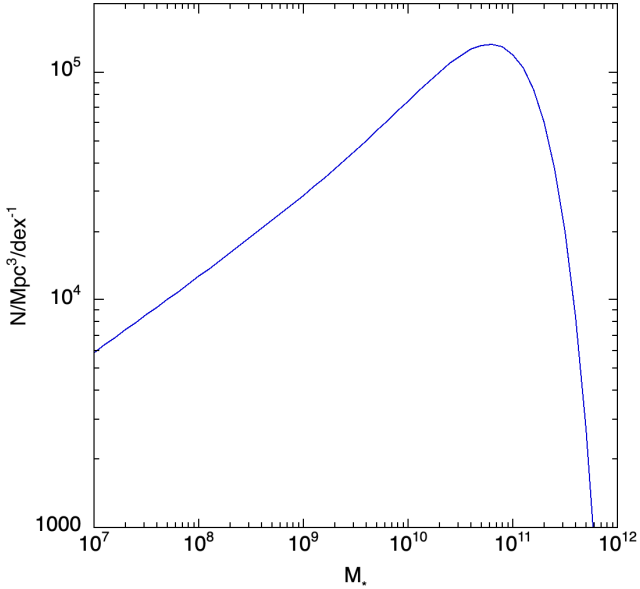


Figure 11. The QSO space density as a function of galaxy stellar mass formed by multiplying the galaxy stellar mass function by essentially the X-ray luminosity-stellar mass relation of Aird et al. (2012). Note the similarity to the QSO space density as a function of halo mass in Fig. 10.

Figure 4 (top left panel) shows the probability, $p(L_X|M_*, z)$ for a galaxy of given stellar mass, M_* , and redshift, z , to host an AGN of X-ray luminosity, L_X found for X-ray emitting AGN in this survey. Although it is clear that there do exist X-ray AGN in low stellar mass galaxies, their numbers are quite small compared to the numbers in high stellar mass galaxies.

From the top left panel of their Fig. 4 with $0.2 < z < 0.6$, we sum over the four L_X bins to find the probability, $p_{AGN}(M_*, z)$, of a galaxy of stellar mass, M_* , hosting an X-ray AGN. Since the relations in the four L_X bins appear approximately parallel, we are justified here in adopting an average slope giving $p_{AGN} \approx M_*^{0.75}$. From Ilbert et al. (2013), their $0.2 < z < 0.5$ stellar mass function in their Fig. 5 is given by their eq (2) with $\log(M_*) = 10.88$, $\phi_{*1} = 1.68 \times 10^{-3} \text{ h}^3 \text{ Mpc}^{-3}$, $\alpha_1 = -0.69$, $\phi_{*2} = 0.77 \times 10^{-3}$ and $\alpha_2 = -1.42$. Multiplying this stellar mass function by the probability, $p_{AGN} \sim M_*^{0.75}$, then gives the number density of AGN as a function of stellar mass as shown in Fig. 11. So for the form of the AGN-stellar mass function we find a peaked distribution, centred on $M_* \approx 6 \times 10^{10} M_\odot$. Essentially the low stellar mass end is cut off by the steep correlation with X-ray luminosity while the AGN space density at high stellar masses is naturally suppressed by the decrease in the galaxy stellar mass function at high masses. We find 67% of the AGN lie in the stellar mass range $10.0 < \log M_*(M_\odot) < 11.5$. Given a halo mass-stellar mass ratio of ≈ 40 at the peak we see that there is reasonable consistency between the QSO halo and stellar mass functions with both implying a relatively small mass range preferred for QSO hosts.

5.6 Evolution of QSO halo mass and luminosity functions

Finally, we consider the question of the physical interpretation of the evolution of the QSO Luminosity Function (LF) which takes a Pure Luminosity Evolution (PLE) form over the range $0 < z < 2.2$ (e.g. Longair 1966; Marshall 1985). Here, QSO luminosity at L^* increases by $\approx (1+z)^3$ or a factor of ≈ 30 by $z = 2.2$. Shanks

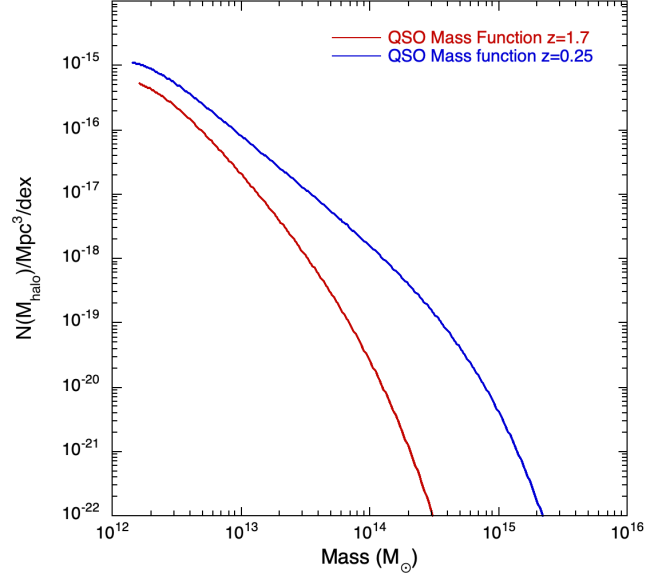


Figure 12. The QSO space density at $z = 1.7$ and $z = 0.25$ as a function of halo mass for our QSO HOD model previously shown in Fig. 8 and with the same HOD parameters as detailed there. The difference between the two models represents the evolution of the halo mass function between these two redshifts which may appear not dissimilar to the Pure Luminosity Evolution shown by the QSO Luminosity Function.

et al. (2011) (see also Marshall 1985; Boyle et al. 1988; Croom et al. 2004, 2009) have speculated that this coherence of the amplitude of the QSO LF over $\approx 10^{10}$ years might demand a coincidence if QSOs only had lifetimes of $10^6 - 10^9$ years, implying that they may be longer-lived. The PLE model also predicts only a slow rise in BH mass between $z = 2.2$ and $z = 0$ despite the sharp decrease in QSO luminosity and again this could be in agreement with the luminosity independence of QSO clustering. However, these authors also noted that the evolution of the QSO correlation function and its implied bias with redshift were not consistent with such a long-lived model (see e.g. Fry 1996). The evolution of the QSO mass function shown in Fig. 12 highlights this issue. Here, taking $b_Q(z = 0.25) = 1.0$ from the $b_Q - z$ fit shown in eq. 15 of Croom et al. (2005), and fitting a HOD to the resulting $\xi_{20}(z = 0.25)$ with $\log(M_{min}) = \log(M_0) = 12.15$, $\sigma_{\log M} = 0.4$, $\log(M_{1'}) = 13.23$ and $\alpha = 0.7$ gives the QSO mass function for $z = 0.25$. This has moved to higher masses compared to the $z = 1.7$ case, taken from Fig. 10(b), as might be expected after gravitational growth, whereas the LF moves to lower luminosities at lower redshift (see e.g. Fig. 6 of Croom et al. 2009). This behaviour of the LF under PLE is sometimes called "downsizing". With lower luminosities and higher masses at low redshifts the Eddington ratios are clearly lower at low redshift. Now despite the opposite direction of the evolution of the mass and luminosity functions, both appear consistent with evolution in the horizontal (mass) direction with the mass function showing roughly constant space densities with redshift, similar to the LF. Since this constant QSO density with redshift seems to appear naturally out of gravitational growth in the Λ CDM model, then no appeal to a long-lived QSO model may be needed to explain the non-evolution of the QSO LF in the density direction. In this case the dimming of the QSO LF with decreasing redshift could be ascribed to depletion of the supply of gas+stars to fuel QSO accretion. The analogy here would be with galaxy evolution if the reason for the observed dimming of

the galaxy LF is depletion of the gas supply, in this case inhibiting star-formation. Although in both cases there would need to be a mechanism invoked to restrict fuel supply while gravitational growth was on-going, this interpretation for QSO PLE seems worth further study, including testing its prediction of QSO M_{BH} independence of redshift and luminosity via (stacked) reverberation mapping analyses.

6 CONCLUSIONS

The aim of this paper was to make new estimates of QSO host halo masses via QSO clustering and QSO-CMB lensing cross-correlation analyses. The QSO catalogues came from the VST-ATLAS quasar survey of Paper I. The depth and reliability of the ATLAS QSO catalogue meant that we could measure the QSO 2-point angular correlation function directly from the data. We found that it was well modelled in 3-D by a correlation function with a power law form, $\xi(r) = (r/r_0)^\gamma$ with $r_0 = 5.2h^{-1}$ Mpc and $\gamma = -1.8$. Then assuming a linear regime mass power spectrum in a Λ CDM model, we compared galaxy and mass auto-correlation functions within a $20h^{-1}$ Mpc radius sphere (i.e. ξ_{20}) to find $b_Q = 2.09 \pm 0.09$ implying a QSO halo mass of $M_{halo} = 8.5 \pm 0.3 \times 10^{11} M_\odot$.

We then cross-correlated the QSO sample described in Sec. 2.1 with the CMB lensing maps of Planck Collaboration et al. (2018). We first used methods similar to those outlined by Geach et al. (2019) to measure the bias and halo mass via the lensing of the CMB by foreground quasars. Here we find good agreement between our data and that of Geach et al. (2019) as well as that of Petter et al. (2022). We are then able to fit the model determined by Geach et al. (2019) to our data with a scaling factor of 0.8 and a scaling factor of 0.85 to the model determined by Petter et al. (2022). Therefore, we are able to measure a quasar halo bias of $b_h = 2.08 \pm 0.3$ at an average redshift of $z = 1.7$, corresponding to a halo mass of $0.83 \times 10^{12} h^{-1} M_\odot$. Our bias value is in excellent agreement with the quasar bias from quasar clustering in Chehade et al. (2016) as well as the QSO-CMB cross-correlation study of Petter et al. (2022).

We then combined these two methods and fitted a HOD model to w_{qq} which could be tested for consistency using QSO-CMB lensing. The HOD parameters that we obtained from w_{qq} were similar to those measured for unobscured QSOs by Petter et al. (2023) with the only difference being that $\log(M_{min})$, $\log(M_0)$, and $\log(M_{1'})$ were $\log(M) = 0.2$ smaller than measured by Petter et al. (2023). From the resulting QSO mass function produced by multiplying the Λ CDM halo mass function by the QSO HOD, we found an average QSO halo mass at $z = 1.7$ of $\log M_{eff} = 12.4$, again about $\log(M) = 0.2$ smaller than measured by Petter et al. (2023) and also slightly higher than measured from b_h inferred directly from w_{qq} and via CMB lensing cross-correlation, w_{qk} . However, this HOD model from our w_{qq} was also found to be a good fit to our CMB lensing results, confirming consistency between these two independent observations. From the QSO mass function we also found that 67% of the $z = 1.7$ QSOs had halo masses that lie in the small halo mass range $12.2 < \log M < 13.15$ suggesting that most QSOs have similar halo and hence black hole masses. A similar result can be found by combining the galaxy stellar mass function of Ilbert et al. (2013) and the probability of a galaxy hosting an X-ray AGN as a function of stellar mass as estimated by Aird et al. (2012). Here, 67% of $z = 1.7$ AGN are found to lie in the stellar mass range $10.0 < \log M_*(M_\odot) < 11.5$.

Finally, we inter-compared the QSO halo mass functions at $z = 0.25$ and $z = 1.7$ and showed that they appear to evolve to higher masses as redshift decreases as would be expected from gravitational

growth. Although the QSO LF evolves in the opposite direction to lower luminosities at low redshift, the two functions otherwise appear similar with the halo mass function evolving mostly in the mass rather than the space density direction. This is reminiscent of the PLE shown by the QSO Luminosity Function. Thus it may be that this constant QSO space density with redshift may be naturally explained by gravitational growth in a Λ CDM Universe with no need to invoke long lived QSO models as discussed by Shanks et al. (2011). In this case the decreasing brightness of QSOs towards the present day may be explained by the increasing lack of material available for accretion to fuel the QSO, despite the gravitational growth of the QSO halo mass. This would then amount to an analogous explanation to the PLE seen in galaxies where the low luminosity of galaxies at low redshift may be due to the reduction in the gas supply needed to fuel star-formation, causing the galaxies to dim in the rest optical bands by the present day (see e.g. Metcalfe et al. 2001).

DATA AVAILABILITY STATEMENT

The ESO VST ATLAS data we have used are all publicly available. The VST ATLAS QSO Catalogue can be found at https://astro.dur.ac.uk/cea/vstatlas/qso_catalogue/. All other data relevant to this publication will be supplied on request to the authors.

ACKNOWLEDGEMENTS

We acknowledge use of the ESO VLT Survey Telescope (VST) ATLAS. The ATLAS survey is based on data products from observations made with ESO Telescopes at the La Silla Paranal Observatory under program ID 177.A-3011(A,B,C,D,E,F,G,H,I,J,K,L,M,N) (see Shanks et al. 2015). BA acknowledges support from the Australian Research Council's Discovery Projects scheme (DP200101068). LFB acknowledges support from ANID BASAL project FB210003. We finally acknowledge STFC Consolidated Grant ST/T000244/1 in supporting this research.

For the purpose of open access, the authors have applied a Creative Commons Attribution (CC BY) licence to any Author Accepted Manuscript version arising.

Finally, we thank the referee for useful comments that improved the quality of this paper.

REFERENCES

- Aird J., et al., 2012, *ApJ*, 746, 90
- Alonso D., 2012, arXiv e-prints, p. arXiv:1210.1833
- Blanchard A., Schneider J., 1987, *A&A*, 184, 1
- Boyle B. J., Shanks T., Peterson B. A., 1988, *MNRAS*, 235, 935
- Bullock J. S., Kolatt T. S., Sigad Y., Somerville R. S., Kravtsov A. V., Klypin A. A., Primack J. R., Dekel A., 2001, *MNRAS*, 321, 559
- Chehade B., et al., 2016, *MNRAS*, 459, 1179
- Croom S. M., Smith R. J., Boyle B. J., Shanks T., Miller L., Outram P. J., Loaring N. S., 2004, *MNRAS*, 349, 1397
- Croom S. M., et al., 2005, *MNRAS*, 356, 415
- Croom S. M., et al., 2009, *MNRAS*, 399, 1755
- Dawson K. S., et al., 2013, *AJ*, 145, 10
- Dey A., et al., 2019, *AJ*, 157, 168
- Eftekhazadeh S., et al., 2015, *MNRAS*, 453, 2779
- Eltvedt A. M., et al., 2023, *MNRAS*, 521, 3384
- Eltvedt A. M., Shanks T., Ansarinejad B., Metcalfe N., Murphy D., 2024, The VST ATLAS Quasar Survey II: Masses of galaxies, Luminous Red Galaxies and galaxy clusters via quasar and CMB lensing, in prep

- Fry J. N., 1996, *ApJ*, 461, L65
- Geach J. E., Peacock J. A., 2017, *Nature Astronomy*, 1, 795
- Geach J. E., Peacock J. A., Myers A. D., Hickox R. C., Burchard M. C., Jones M. L., 2019, *ApJ*, 874, 85
- Han J., Ferraro S., Giusarma E., Ho S., 2019, *MNRAS*, 485, 1720
- Ilbert O., et al., 2013, *A&A*, 556, A55
- Jain B., Scranton R., Sheth R. K., 2003, *MNRAS*, 345, 62
- Kaiser N., 1987, *MNRAS*, 227, 1
- Landy S. D., Szalay A. S., 1993, *ApJ*, 412, 64
- Limber D. N., 1953, *ApJ*, 117, 134
- Longair M. S., 1966, *MNRAS*, 133, 421
- Marshall H. L., 1985, *ApJ*, 299, 109
- Metcalfe N., Shanks T., Campos A., McCracken H. J., Fong R., 2001, *MNRAS*, 323, 795
- Murray S. G., Diemer B., Chen Z., Neuhold A. G., Schnapp M. A., Peruzzi T., Blevins D., Engelman T., 2021, *Astronomy and Computing*, 36, 100487
- Navarro J. F., Frenk C. S., White S. D. M., 1996, *ApJ*, 462, 563
- Peebles P. J. E., 1980, *The large-scale structure of the universe*. Princeton University Press
- Petter G. C., et al., 2022, *ApJ*, 927, 16
- Petter G. C., Hickox R. C., Alexander D. M., Myers A. D., Geach J. E., Whalen K. E., Andonie C. P., 2023, *ApJ*, 946, 27
- Phillipps S., Fong R., Ellis R. S., Fall S. M., MacGillivray H. T., 1978, *MNRAS*, 182, 673
- Planck Collaboration et al., 2018, arXiv e-prints, p. arXiv:1807.06210
- Scranton R., et al., 2005, *ApJ*, 633, 589
- Seljak U., 1996, *ApJ*, 463, 1
- Shanks T., Croom S. M., Fine S., Ross N. P., Sawangwit U., 2011, *MNRAS*, 416, 650
- Shanks T., et al., 2015, *MNRAS*, 451, 4238
- Tinker J. L., Robertson B. E., Kravtsov A. V., Klypin A., Warren M. S., Yepes G., Gottlöber S., 2010, *ApJ*, 724, 878
- Williams L. L. R., Irwin M., 1998, *MNRAS*, 298, 378
- Zheng Z., Weinberg D. H., 2007, *ApJ*, 659, 1

This paper has been typeset from a $\text{\TeX}/\text{\LaTeX}$ file prepared by the author.